J|A|C|S
ARTICLES
Published on Web 02/02/2006

Creating Polymer Structures of Tunable Electric Functionality by Nanoscale Discharge-Assisted Cross-Linking and Oxygenation

Xian Ning Xie,*[,†] Mu Deng,[†] Hai Xu,[‡] Shuo Wang Yang,[§] Dong Chen Qi,[†,‡] Xing Yu Gao,[‡] Hong Jing Chung,[†,‡] Chorng Haur Sow,[†,‡] Vincent B. C. Tan,[†,⊥] and Andrew Thye Shen Wee*[,†,‡]

Contribution from the NUS Nanoscience and Nanotechnology Initiative (NUSNNI), National University of Singapore, Department of Physics, National University of Singapore, 2 Science Drive 3, Singapore, 117542, Institute of High Performance Computing (IHPC), 8 Science Park 2, Singapore, 117542, and Department of Mechanical Engineering, National University of Singapore, Singapore, 117576

Received November 13, 2005; E-mail: phyweets@nus.edu.sg (A.T.S. Wee); nnixxn@nus.edu.sg (X.N. Xie)

Abstract: We report the creation of polymeric micro/nanostructures which exhibit distinct chemical and physical characteristics from the matrix poly(*N*-vinyl carbazole) (PVK). The structure formation is based on atomic force microscopy (AFM) facilitated cross-linking and oxygenation. The reaction of PVK with AFM lithographically induced nanoscale discharge produces raised structures in which bridge oxygen links neighboring carbazole groups. The cross-linking by bridge oxygen converts the initially insulating PVK matrix to chemically modified conducting patterns through the formation of extended π-conjugations. A comprehensive AFM, PES (photoelectron spectroscopy), FTIR (Fourier transform infrared spectroscopy), and DFT (density functional theory) analysis is presented to address the chemophysical identity of the patterned structures. Our results demonstrate new capabilities of AFM nanolithography in generating heterogeneous functional structures in a polymer matrix.

Introduction

Materials patterning and modification is a key process in functional structure formation and device fabrication. Numerous patterning techniques, such as electron- and photolithography,[1,2] laser lithography,[3] and ion beam lithography,[4] have been demonstrated for creating two- and three-dimensional structure on various materials. The recent development of AFM nanolithography[5−20] has substantially added new capabilities to conventional lithographical techniques. The direct view of features and control of tip motion at the nanoscale make AFM nanolithography especially useful in generating site-specific and localized structures. Basically, AFM nanolithography can be classified into two categories in terms of the chemophysical identity of the structures formed. In the first category, the structures are created without modifying or changing the chemical composition of the matrix materials. Typical examples include dip-pen nanolithography (DPN),[5−7] and thermomechanical indentation, etc.[8−10] In DPN,[5−7] the patterns are written by transferring molecules (inks) from the tip (pen) to substrates. The deposited structures essentially maintain the same chemical structure and functionality of the original inks. As for thermomechanical indentation,[8−10] the data storage units were fabricated by physically removing polymeric materials to form pits with memory functions. In the second category, the materials patterning proceeds via certain chemical reactions or modifica-

[†] NUS Nanoscience and Nanotechnology Initiative (NUSNNI).
[‡] Department of Physics.
[§] Institute of High Performance Computing (IHPC).
[⊥] Department of Mechanical Engineering.

(1) Wei, Y. Y.; Eres, G. *Appl. Phys. Lett.* **2000**, *76*, 194.
(2) Goodberlet, J. G. *Appl. Phys. Lett.* **2000**, *76*, 667.
(3) Georgiev, D. G.; Baird, R. J.; Avrutsky, I.; Auner, G.; Newaz, G. *Appl. Phys. Lett.* **2004**, *84*, 4881.
(4) Teo, E. J.; Breese, M. B. H.; Tavernier, E. P.; Bettiol, A. A.; Watt, F.; Liu, M. H.; Blackwood, D. J. *Appl. Phys. Lett.* **2004**, *84*, 3202.
(5) Demers, L. M.; Ginger, D. S.; Park, S.-J.; Li, Z.; Chung, S.-W.; Mirkin, C. A. *Science* **2002**, *296*, 1836.
(6) Lee, K.-B.; Park, S.-J.; Mirkin, C. A.; Smith, J. C.; Mrksich, M. *Science* **2002**, *295*, 1702.
(7) Agarwal, G.; Sowards, L. A.; Naik, R. R.; Stone, M. O. *J. Am. Chem. Soc.* **2003**, *125*, 580.
(8) Durig, U.; Cross, G.; Despont, M.; Drechsler, U.; Haberle, W.; Lutwyche, M. I.; Rothuizen, H.; Stuts, R.; Widmer, R.; Vettiger, P.; Binnig, G. K.; King, W. P.; Goodson, K. E. *Tribol. Lett.* **2002**, *9*, 25.
(9) Lutwyche, M. I.; Despont, M.; Drechsler, U.; Durig, U.; Haberle, W.; Rothuizen, H.; Stutz, R.; Widmer, R.; Binnig, G. K.; Vettiger, P. *Appl. Phys. Lett.* **2000**, *77*, 3299.
(10) King, W. P.; Kenny, T. W.; Goodson, K. E.; Cross, G.; Despont, M.; Durig, U.; Rothuizen, H.; Binnig, G. K.; Vettiger, P. *Appl. Phys. Lett.* **2001**, *78*, 1300.
(11) Snow, E. S.; Campbell, P. M. *Science* **1995**, *270*, 1639.
(12) Xie, X. N.; Chung, H. J.; Xu, H.; Xu, X.; Sow, C. H.; Wee, A. T. S. *J. Am. Chem. Soc.* **2004**, *126*, 7665.
(13) Tello, M.; Garcia, R. *Appl. Phys. Lett.* **2001**, *79*, 424.
(14) Hoeppener, S.; Maoz, R.; Cohen, S. R.; Chi, L. F.; Fuchs, H.; Sagiv, J. *Adv. Mater.* **2002**, *14*, 1036.
(15) Tully, D. C.; Trimble, A. R.; Frechet, J. M. J. *Adv. Mater.* **2000**, *12*, 1118.
(16) Tully, D. C.; Wilder, K.; Frechet, J. M. J.; Trimble, A. R.; Quate, C. F. *Adv. Mater.* **1999**, *11*, 314.
(17) Suez, I.; Backer, S. A.; Frechet, J. M. J. *Nano Lett.* **2005**, *5*, 321.
(18) Tello, M.; Garcia, R.; Martin-Gago, J. A.; Martinez, N. F.; Martin-Gonzalez, M. S.; Aballe, L.; Baranov, A.; Gregoratti, L. *Adv. Mater.* **2005**, *17*, 1480.
(19) Martinez, R. V.; Garcia, R. *Nano Lett.* **2005**, *5*, 1161.
(20) Mori, G.; Lazzarino, M.; Ercolani, D.; Sorba, L.; Heun, S. *J. Appl. Phys.* **2005**, *97*, 114324.

10.1021/ja0577241 CCC: $33.50

tions such that the structures produced exhibit distinct chemophysical characteristics from those of the raw materials. For example, anodic oxidation[11−13] creates gate oxides which are insulating as opposed to the metal or semiconducting substrates, and these oxides can be used as dielectric barriers to modulate electron conduction. In the oxygenation of self-assembled monolayers (SAM),[14] the $-CH_3$ terminals of alkyl chains were oxidized to −COOH groups by tip-induced local potentials, and the resultant −COOH groups could facilitate the hierarchical layer-by-layer construction of SAMs for metallic cluster attachment. Besides metals, semiconductors, and organic molecules, AFM was also employed to oxidize dendritic polymer monolayer and deposit etch-resistant materials.[15−17] Most recently, several authors reported the nanoscale structuring by AFM probe-assisted formation and manipulation of organic menisci.[18,19] Characterization of the physicochemical properties of oxide structures fabricated by AFM anodic oxidation was further conducted using different techniques.[20,21]

Poly(*N*-vinyl carbazole) (PVK) is a photorefractive polymer which has widespread applications in xerography. The native PVK contains saturated hydrocarbon backbones and aromatic carbazole pendants forming a helical structure. PVK is a good polymeric insulator with a HOMO (highest occupied molecular orbital) and LUMO (lowest unoccupied molecular orbital) gap of 3.5 eV.[22] Due to the electron-donating behavior of the carbazole groups, PVK is used as a hole-transport layer in organic light-emitting diodes (OLED).[22,23] Moreover, the hole conduction in PVK can be converted to electron conduction by doping it with other materials to form charge-transfer complexes.[24,25] While previous work concerns PVK-based materials modification and device fabrication on a large scale,[22−25] the miniaturization of devices would eventually require that functional structures be defined locally at the nanoscale.[8−10] In this context, we carried out AFM nanolithography on PVK with the aim to produce heterogeneous structures for micro/nanoscale material engineering and patterning. Raised patterns were grown on PVK through the chemical reaction of polymer with air discharge generated in the tip−PVK gap under high electric fields. Conducting AFM (cAFM), photoelectron spectroscopy (PES), and Fourier transform infrared spectroscopy (FTIR) measurements, combined with density functional theory (DFT) calculations, were performed to identify the chemical and physical characteristics of the polymeric structures. The PVK patterns exhibit a unique chemical configuration in which the carbazole groups of neighboring chains are cross-linked by bridge oxygen. The cross-linking and oxygenation significantly modifies the electric functionality of the materials, leading to the formation of conducting structures on the initially insulating matrix PVK.

Experimental Section

Preparation of PVK Films and AFM Experiments. Poly(*N*-vinyl carbazole) (PVK, MW = 1100 k) was purchased from Aldrich and used without further purification. Si (100) substrates were sonicated in ethanol, rinsed with acetone, and blow-dried in N_2 gas. The PVK films were prepared by spin-coating 0.5 wt % PVK solution in toluene onto Si substrates followed by annealing in a vacuum oven for 2 h at ∼175 °C. The thickness of the PVK films is ∼40 nm, as determined by atomic force microscopy (AFM) technique. A NanoMan AFM system (Nanoscope IV, Veeco Inc.) was operated in air for all the AFM-based patterning and measurements.[26,27] Silicon nitride (Si_3N_4) contact tips were home-coated with ultrathin gold (Au) layers using an electron beam evaporator. The AFM tip was engaged with the substrate with a typical spacing of 1−5 nm, immobilized at selected surface sites. A negative tip bias (relative to the sample) was applied for certain durations to initiate the local patterning of PVK. To collect the current map using conductive AFM (cAFM), a scanning voltage was applied to record both the morphology and current images simultaneously for the patterned structures. For current−voltage ($I-V$) data collection, the motionless tip was located at the desired sites, the voltage was ramped, and the corresponding current was detected by an internal current sensor (with picoamp to microamp sensitivity) in the AFM system. Lower voltages were used in current mapping to avoid possible modification of the PVK films. When bias voltages >12 V were needed, an external Keithley 237 dc power supply was integrated to the AFM system to facilitate the patterning under higher voltages.[26]

PES, FTIR Characterizations and DFT Calculations. PES characterization of PVK was carried out at the end station attached to the surface and interface nanostructures (SINS) beam line at the Singapore synchrotron light source (SSLS), National University of Singapore.[28] The photoelectron was activated by p-polarized light, and the spectra were recorded with a hemispherical electron energy analyzer (EA 125, Omicron NanoTechnology GmbH.). The electron energy resolution in the form of $E/\Delta E$ was about 1000 for the photon energies used in the experiments. Fourier transform infrared spectroscopy (FTIR) spectra were acquired using a SHIMAZU AIM-8800 infrared spectrometry. The signals were recorded in reflection mode with an MCT detector which is cooled by liquid nitrogen. A scan range of 400−4000 cm^{-1} was chosen, and the scan step was set to 4 cm^{-1}. Density functional theory (DFT) calculation was carried out using DMol^3 quantum mechanical code (Accelrys Inc.). The electron wave functions were expanded in terms of the Gaussian 6-31G** basis set. The generalized gradient approximation (GGA) in the level of PW91 was employed in the calculation of equilibrium geometry and formation energy.

Results and Discussion

Figure 1a shows the AFM image of a typical pattern generated on PVK by applying a 10 V tip bias for 1 s (second). The structure is characterized by a raised central cone surrounded by an outer ring. The cone is ∼15 nm high and ∼220 nm wide (full width at half-maximum). The diameter and maximum height of the outer ring are ∼1.2 μm and ∼4 nm, respectively. The formation of such central and outer structures was also observed on other materials and is attributable to the initiation of nanoscale discharge and transient shock waves in ambient air.[29] As illustrated in Figure 1b, the applied high field (10^7-10^{10} V/m) could initiate the ionization of ambient air in the nanometer-sized tip−PVK gap (1−5 nm) to trigger a nanoscale discharge or explosion. Due to the explosive nanodischarge, transient shock waves are generated in the air gap. On the basis

(21) Xie, X. N.; Chung, H. J.; Sow, C. H.; Wee, A. T. S. *Appl. Phys. Lett.* **2005**, *86*, 192904.
(22) de Morais, T. D.; Chaput, F.; Lahlil, K.; Boilor, J.-P. *Adv. Mater.* **1999**, *11*, 107.
(23) Kido, J.; Shionoya, H.; Nagai, K. *Appl. Phys. Lett.* **1995**, *67*, 2281.
(24) Gill, W. D. *J. Appl. Phys.* **1972**, *43*, 5033.
(25) Zhang, Y.; Hu, Y.; Chen, J.; Zhou, Q.; Ma, D. *J. Phys. D: Appl. Phys.* **2003**, *36*, 2006.
(26) Xie, X. N.; Chung, H. J.; Sow, C. H.; Bettiol, A. A.; Wee, A. T. S. *Adv. Mater.* **2005**, *17*, 1386.
(27) Xie, X. N.; Chung, H. J.; Sow, C. H.; Wee, A. T. S. *Appl. Phys. Lett.* **2005**, *86*, 023112.
(28) Yu, X. J.; Wilhelmi, O.; Moser, H. O.; Vidyaraj, S. V.; Gao, X. Y.; Wee, A. T. S.; Nyunt, T.; Qian, H. J.; Zheng, H. W. *J. Electron Spectrosc. Relat. Phenom.* **2005**, *144*, 1031.
(29) Xie, X. N.; Chung, H. J.; Sow, C. H.; Adamiak, K.; Wee, A. T. S. *J. Am. Chem. Soc.* **2005**, *127*, 15562.

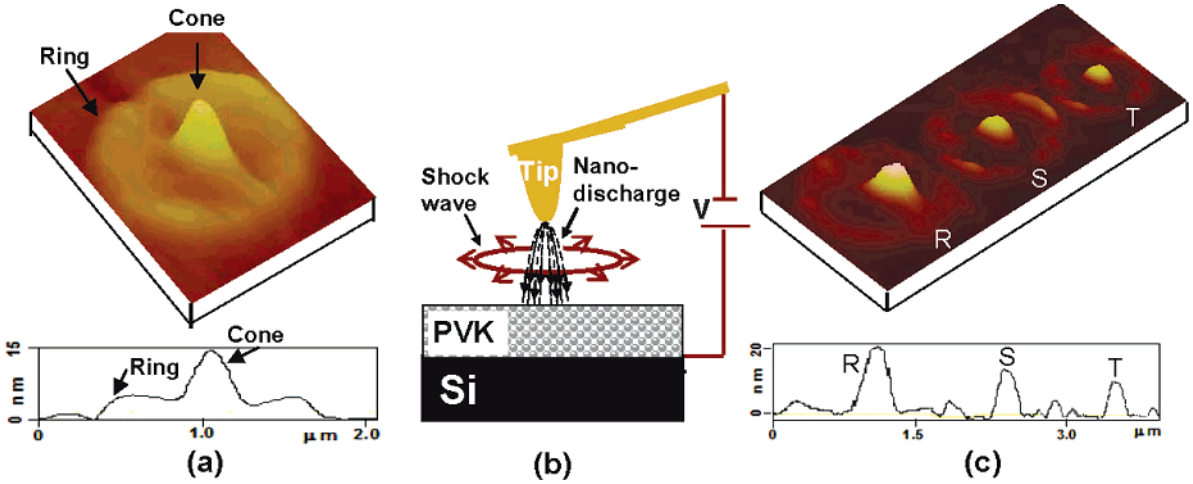

Figure 1. (a) Raised central cone and outer ring formation on PVK by applying a 10 V tip bias for 1 s duration. (b) Proposed nanodischarge and shock wave generation for the formation of the central and outer structures. (c) Central and outer structures R, S, and T produced by maintaining different tip voltages of 12, 10, and 8 V for the same duration, respectively.

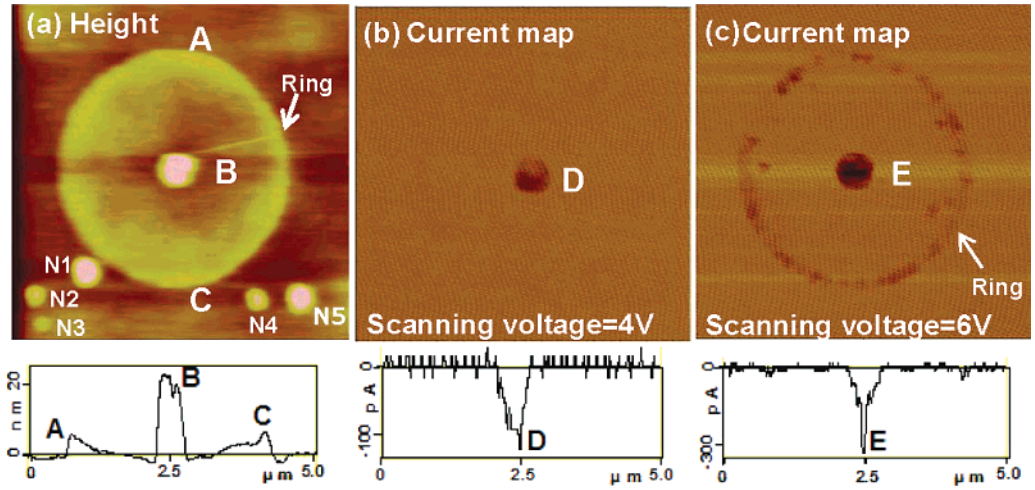

Figure 2. (a) AFM morphology image of a central and outer structure produced with 12 V tip voltage. The dots N1−N5 outside the ring are native dots initially present on the PVK film before AFM patterning. (b) AFM current image of (a) recorded simultaneously with a scanning voltage of 4 V. (c) AFM current image of (a) recorded with a scanning voltage of 6 V.

of our simulation, the nanodischarge is confined in the vicinity of the tip apex, and the electric field and charge density distribution is highly localized inside the discharge zone as shown in Figure 1b.[29] Therefore, the formation of the raised central cone arises from the stronger electric field and higher charge density near the tip apex. For the discharge geometry considered in Figure 1b, the shock front would be centered at the tip apex and will propagate along directions parallel to the PVK surface. The radial propagation of the shock front can significantly expand the trajectory of ionized particles out of the central discharge zone, leading to the formation of the microscale outer ring.[29] It is noticed in Figure 1a that there are regions between the central cone and outer ring which show lower density of reactive species (indicated by their lower height in morphology). This could be due to the reduction/depletion of the charge density in the rarefied region generated in the course of nanoexplosion and shock wave propagation. Figure 1c exhibits three similar structures, R, S, and T, produced with 12, 10, and 8 V bias for the same bias duration, respectively. It can be seen that the height of the central cones and diameter of the outer rings decreases with the lowering of tip voltage. This indicates the correlation between tip voltage (or electric field) and the strength of nanoexplosion: higher tip voltage facilitates stronger local discharge and larger shock front propagation.

The local electrical property of the PVK patterns was further probed using conductive AFM (cAFM).[27] Figure 2a shows the AFM morphology of a central cone and outer ring. Sites N1−N5 outside the ring are native dots initially present on PVK before AFM patterning. Among them, dots N1 and N5 are comparable in height and diameter to the central cone B generated by AFM-induced nanodischarge. Figure 2b exhibits the current mapping of these structures recorded simultaneously with the morphology shown in Figure 2a. A conductive site D is visible in the center of the current image, and it corresponds to the central cone B in the morphological image shown in Figure 2a. At a scanning voltage of 4 V, the maximum current detected for site D is ∼100 pA (negative value due to tip negative polarity) higher than that of the insulating background. When the scanning voltage was raised to 6 V, the current from the central cone increased to ∼300 pA (see site E in Figure 2c). In addition, electric current was also measured at the edge of the outer ring. No current was detected at the native sites N1−N5, although these protruding dots are similar in vertical

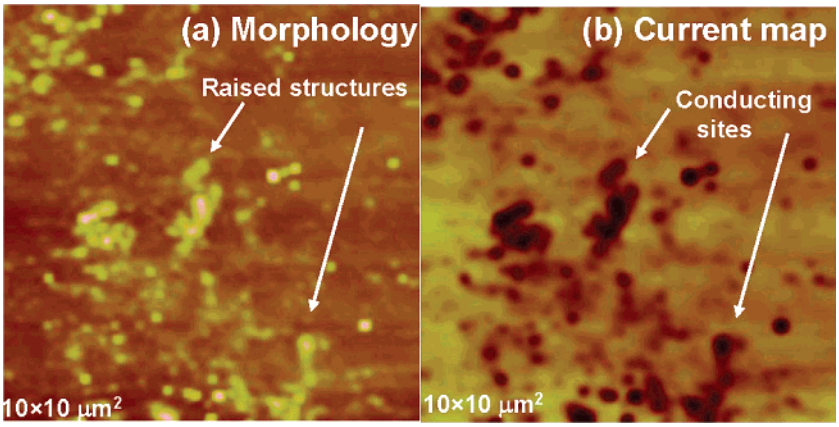

Figure 3. (a) AFM morphology and (b) current map recorded for PVK samples exposed to large-scale discharge in ambient air. The raised PVK structures observed in (a) correspond to the conducting sites in (b). A scanning voltage of 6 V was used to obtain the current image.

dimension to the central cone and outer ring shown in Figure 2a.

We now address the formation mechanism and origin of electrical conductivity for the central cone and outer ring. The observations in Figures 1 and 2 suggest that the patterns are most probably the products of chemical reactions between the explosive nanodischarge and PVK, and the resulting structures are chemophysically different from the raw PVK. To confirm this, we exposed native PVK samples to large-scale air discharge generated by a tabletop Van de Graaff generator (VDG) (see Supporting Information S1). The discharge conditions were kept comparable to those in the nanodischarge, except that the area of reacted PVK was large enough (~4 mm in diameter) for FTIR and PES characterizations. Figure 3, parts a and b, displays the typical AFM morphology and current images recorded for PVK samples exposed to large-scale discharge in ambient air. Before discharge exposure, the PVK surface is relatively flat, and the statistical coverage of native dots present on the surface is less than 7%. After discharge exposure, many raised dotlike structures (1−16 nm in height) were formed on PVK surface (see Figure 3a), leading to a significant increase in the surface coverage of the raised structures. On the basis of our AFM results, a surface coverage of more than 50% was estimated for the discharge-exposed samples. Therefore, these newly formed structures can be mainly attributed to the reaction products between the discharge and PVK, and considered to be comparable to those patterns shown in Figure 1. In Figure 3b, the raised sites exhibit higher conductivity; the maximum current measured for the conductive sites is ~230 pA more than the flat background. These results suggest that there are similar chemical reactions leading to the formation of conducting structures on PVK samples exposed to AFM-based nanodischarge and large-scale discharge, respectively.

In Figure 4a, we compare the FTIR spectra recorded in the 1230−1250 cm^{-1} range for the discharge-exposed and unexposed PVK regions. Two peaks at 1236 and 1247 cm^{-1} were identified for the exposed PVK, while no vibration modes were detected on the unexposed PVK sample. The two peaks at 1236 and 1247 cm^{-1} are attributable to the vibration frequency of the diphenyl ether group (Ph−O−Ph), and this assignment is consistent with the literature[30] and our calculations based on density functional theory (DFT). The FTIR results suggest that the carbazole groups in the discharge-exposed PVK are cross-linked by bridge oxygen. Further comparison of PES data confirmed the formation of bridge oxygen in PVK patterns. As seen in Figure 4b, the unexposed PVK shows an O 1s core level emission at 532.9 eV, which corresponds to the amorphous native silicon oxides and hydroxide present on the Si substrate.[31] The O 1s peak recorded for discharge-exposed PVK is larger in area and shifted to higher binding energy (BE). After subtracting the smaller background peak from the larger one, we obtained a difference spectrum with a peak centered at 533.6 eV. This peak can be considered to be the O 1s emission from the reacted PVK only and can be unambiguously assigned to the Ph−O−Ph bridge oxygen. As seen in Figure 4c, our DFT calculation shows that the 2p states of the Ph−O−Ph bridge oxygen overlap with the π-states of the benzene rings. The delocalization of the valence states of the bridge oxygen would raise the HOMO of PVK by up to 0.8 eV as compared to that of native silicon oxides, thus leading to the shift of O 1s emission toward higher BE as observed in Figure 4b. In addition, C 1s and N 1s PES spectra were also recorded, and within experimental error, only negligible difference was found between the discharge-exposed and unexposed PVK samples (see Supporting Information S2). The results shown in Figure 4 allow us to propose that the pattern formation is due to AFM nanodischarge-induced cross-linking and oxygenation of PVK. The cross-linking of PVK through hydrogen dissociation under electrochemical conditions has been reported previously,[32] whereby the neighboring carbazole groups react to form a dicarbazyl structure through 3,3′-coupling and hydrogen radical releasing. The polymeric entity produced under such conditions does not contain any bridge oxygen to link the carbazyl pedants. In our case, the oxygen ions (e.g., O^- and O_2^-) and radicals (e.g., O*)[33] generated in the nanodischarge react with the native PVK to form bridge oxygen connecting the carbazole groups (see Figure 4d for proposed reactions). The incorporation of extra oxygen atoms into the raw PVK also causes a volume expansion in the reaction products; therefore, raised patterns are formed as shown in Figure 1. The PVK volume increase due to pattern formation

(30) Pouchert, C. J. *The Aldrich Library of Infrared Spectra*, 3rd ed.; Aldrich Chemical Company, Inc., 1981.

(31) Moulder, J. F.; Stickle, W. F.; Sobol, P. E.; Bomben, K. P. *Handbook of X-ray Photoelectron Spectroscopy*; Chastain, J., King, R. C., Jr., Eds.; Physical Electronics, Inc., 1995.
(32) Liu, J. F.; Yang, K. Z.; Lu, Z. H. *J. Am. Chem. Soc.* **1997**, *119*, 11061.
(33) Lachaud, S.; Loiseau, J. F.; Gonbeau, D. *Eur. Phys. J.: Appl. Phys.* **2005**, *29*, 99.

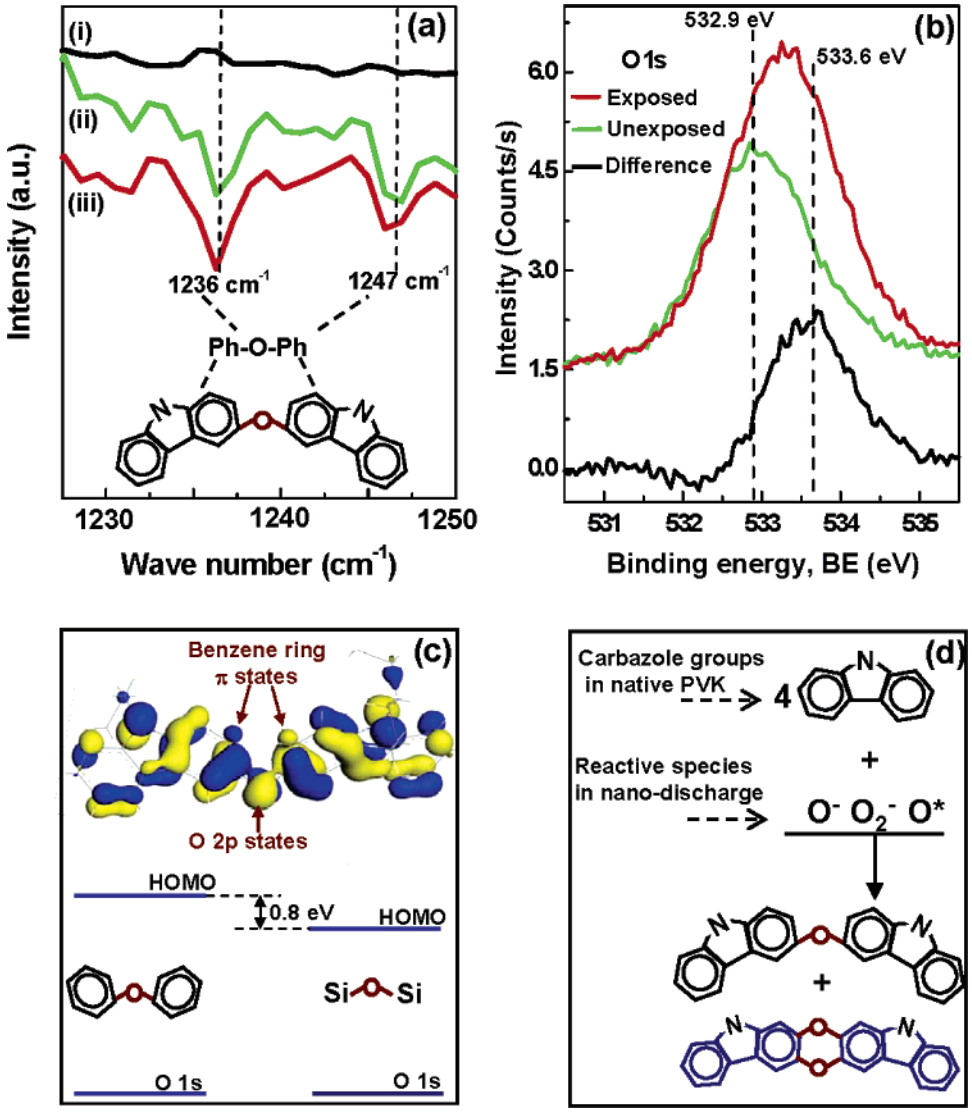

Figure 4. (a) FTIR spectra collected for PVK samples (i) unexposed and (ii) exposed to discharges. Spectrum (iii) is the calculated vibration frequency for the Ph−O−Ph configuration in the cross-linked carbazole groups shown below. (b) PES spectra of O 1s core level emission recorded for PVK samples unexposed and exposed to discharges, respectively. The difference spectrum of the two peaks is also shown. The spectra were obtained with photons of energy $h\nu = 649.2$ eV. (c) Top: calculated HOMO for the structure displayed in (a) showing the overlap of the O 2p states with the π-states of the benzene ring. Bottom: comparison of HOMO levels calculated for cross-linked PVK (left) and silicon oxide (right). The O 1s core level was assumed to be the same in the two molecules. (d) Proposed reactions between the nanodischarge and native PVK for the production of cross-linked carbazole groups by one or two bridge oxygens.

was estimated using the AFM "localized depth" analysis method by comparing the volumes between the reference and sampling squares. The reference square was chosen on the native PVK surface, while the sampling square, which has the same lateral dimension (from 1×1 μm^2 to 4×4 μm^2, depending on the diameter of the outer rings) as the reference square, was positioned to enclose the central and outer PVK patterns. The thickness of the reference square is 40 nm (initial film thickness), and the average thickness of the sampling/patterned area was determined to be 42.6−45.2 nm. Therefore, the volume expansion coefficient was estimated to be 1.06−1.13. This value is in good agreement with the theoretical coefficient of 1.02−1.08 obtained by considering different degree of PVK cross-linkage in DFT calculations. When the patterning experiments were conducted under lower humidity and inert gas flow (e.g., Ar or N_2 gas), the formation of the central and outer structures was not observed due to the absence of reactive oxygen species in the tip−PVK gap.

The impact of cross-linking and oxygenation on the electric functionality of PVK patterns was further investigated by calculating the HOMO−LUMO gap of various configurations. Figure 5, parts a and b, shows the variations of energy gap and the corresponding six structures modeled in our DFT calculations, respectively. Six configurations were considered, including the native PVK (structure i), cross-linked PVK without oxygen (structure ii), and cross-linked PVK with bridge oxygen (structures iii−vi). Among them, structure i of native PVK shows the widest gap of 3.3 eV, which is close to the experimental value of 3.5 eV.[22] The cross-linking in structure ii without oxygen, which was previously produced by electrochemical polymerization,[32] slightly lowers the gap by 0.24 eV. The cross-linking of carbazole groups by one bridge oxygen shown in structure iii lowers the gap by 0.42 eV. As mentioned in Figure 4c, the 2p states of bridge oxygen overlap with the π-states of the benzene rings, thus forming large π-conjugations in the patterned PVK. The extended conjugation helps narrow

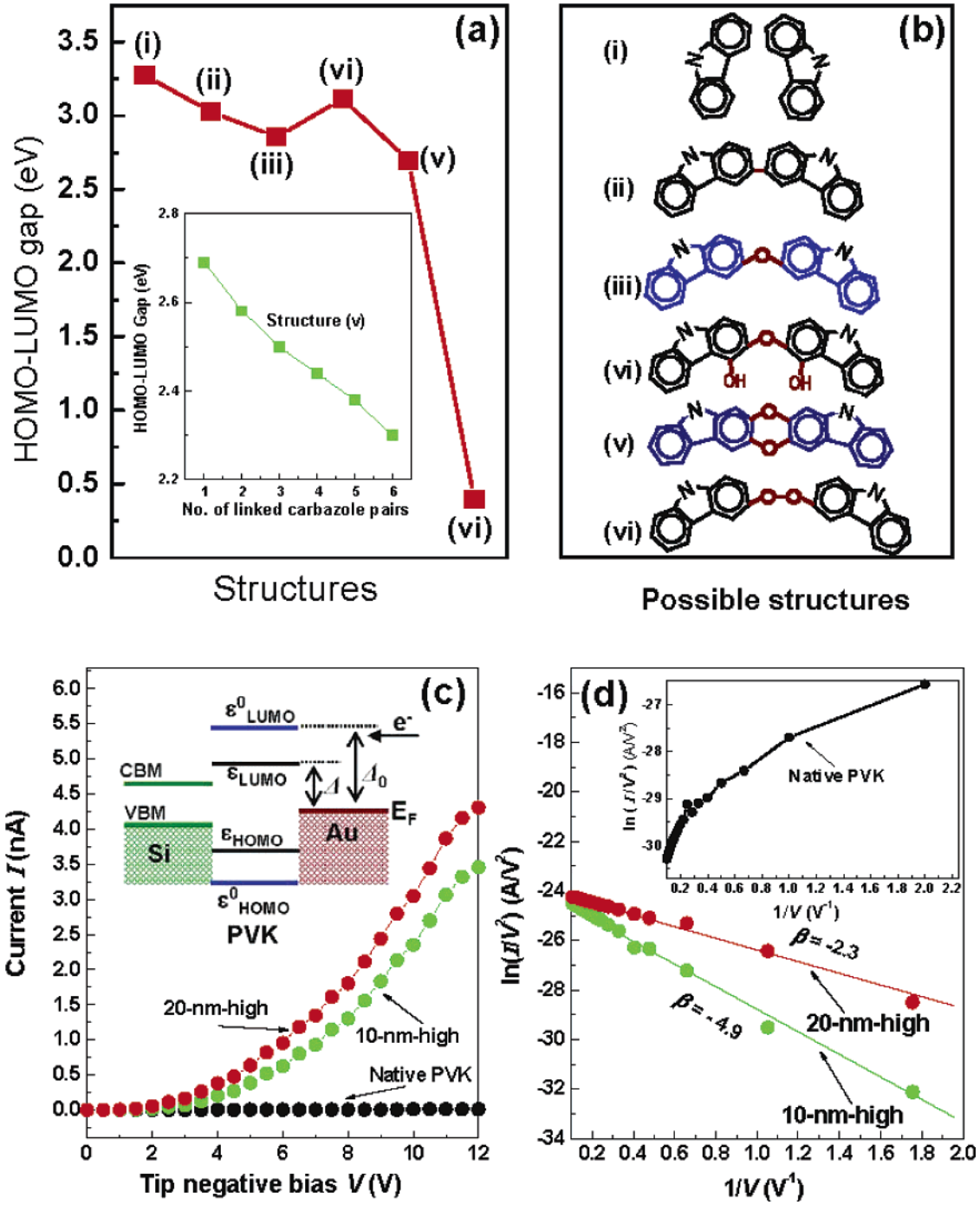

Figure 5. (a) Calculated HOMO−LUMO gap for structures shown in (b). The inset shows the further gap narrowing with increased number of cross-linked carbazole pairs in structure v. (c) $I-V$ curves collected for 20-nm high and 10-nm high PVK patterns and native PVK, respectively. The inset shows the energy diagram of the Si/PVK/Au (tip) configuration used in AFM $I-V$ measurements. ϵ^0_{LUMO}, ϵ^0_{HOMO} and Δ_0 denote the LUMO, HOMO, and tunneling barrier of native PVK, while ϵ_{LUMO}, ϵ_{HOMO}, and Δ denote the LUMO, HOMO, and tunneling barrier of the PVK patterns. (d) Linear $\ln(I/V^2) \sim 1/V$ plots of the $I-V$ curves shown in (c). The solid circles are experimental data, and the solid lines are the fitted linearity with a slope of β. The inset displays the $\ln(I/V^2) \sim 1/V$ plot for native PVK.

the gap by lifting up the HOMO and lowering down the LUMO. If oxygen is attached to the carbazole benzene ring in the form of nonbridge oxygen (e.g., −OH) as shown in structure iv, the gap would be widened, as the nonbridge oxygen degrades the conjugation by reducing the overlap between O 2p states and benzene π-states. The incorporation of the second bridge oxygen as shown in structure v further narrows the energy gap to 2.7 eV. The gap for the configuration of Ph−O−O−Ph peroxide bridge in structure vi was calculated to be only 0.4 eV. However, this configuration is unlikely to be present, or is negligibly low in concentration, in the patterned PVK, as the FTIR and PES spectra characteristic of the Ph−O−O−Ph peroxide were not observed in our experiments. DFT calculations also showed the instability of this structure in terms of formation energy. On the basis of FES, FTIR, and DFT results, the most probable configuration units in the produced PVK patterns are structures iii and v containing one and two Ph−O−Ph bridges as shown in Figure 5b. It should be noted that the above gap values were obtained by considering the cross-linkage of one out of six pairs of carbazoles in structures i−vi (only one pair of carbazoles is

drawn in Figure 5b). When more carbazole pairs were linked in the models, further reduction of the HOMO−LUMO gap was observed. The inset of Figure 5a displays the gap reduction with increased number of cross-linked carbazole pairs in structure v. It can be seen that when the six carbazole pairs are all cross-linked, the gap would be reduced to 2.3 eV. In principle, if more cross-linkage is included in the structures, it is possible to obtain a gap value of <2.0 eV, as the increased number of π-conjugated bonds can significantly reduce the HOMO−LUMO gap of organic molecules.[34] We were unable to determine the gap for structures with ≥7 linked carbazole pairs, as the time cost for computing such large molecules is formidable for our ab initio DFT calculations. Nevertheless, the evolution shown in the inset of Figure 5a clearly indicates the general trend of gap reduction with increased degree of cross-linkage.

Figure 5c displays the typical current−voltage ($I-V$) curves of PVK patterns of different heights collected under conditions without initiating the nanodischarge. It is evident that the current level of the 20-nm high structure is higher than that of the 10-nm high structure, and both the curves exhibit an exponential growth when the tip bias is increased to >4 V. In contrast, the current of the native PVK is much lower than that of the PVK patterns, and the $I-V$ response does not follow the exponential rise. To elucidate the conduction mechanism of the PVK patterns, we considered several possible models, such as Richardson−Schottky (R−S)[35] thermionic emission, Poole−Frenkel (P−F)[36] emission, and Fowler−Nordheim (F−N)[37] tunneling. We found that the F−N model could provide a good description of our experimental data. In the Fowler−Nordheim (F−N) model, the relation between the current density J and electric field E can be expressed as[37]

$$J/E^2 = A\exp(-\beta/E) \tag{1}$$

The parameters A and β are defined to be

$$A = q^3/8\pi h\Delta \tag{2}$$

$$\beta = 8\pi\sqrt{2m_e^*}\Delta^{3/2}/3hq \tag{3}$$

where h, q, Δ, and m_e^* are the Plank's constant, electronic charge, barrier height, and effective electronic mass in the PVK structure. In an F−N plot of $\ln(J/E^2) \sim 1/E$, eq 1 is represented by a straight line whose slope β is related to barrier height Δ in the form of

$$\beta \propto \Delta^{3/2} \tag{4}$$

In our data fitting, we used the modified F−N plot[38,39] of $\ln(I/V^2) \sim 1/V$ where I and V are the electrical current and tip negative bias, respectively. As with the $\ln(J/E^2) \sim 1/E$ plot, the $\ln(I/V^2) \sim 1/V$ plot is also linear and the barrier height Δ can be calculated using eq 4. Figure 5d displays the modified F−N plots of $\ln(I/V^2) \sim 1/V$ for the $I-V$ curves shown in Figure 5c. It can be seen that the $\ln(I/V^2) \sim 1/V$ plots exhibit a linearity which is in good agreement with the predication of the F−N law. Using the relation of $\Delta_1/\Delta_2 = (\beta_1/\beta_2)^{2/3}$, we could obtain the relative barrier height Δ_1/Δ_2 between PVK patterns of different height h_1 and h_2, respectively. As illustrated in the energy diagram shown in the inset of Figure 5c, Δ is the barrier height for electron injection from the tip (Au) to PVK and can be expressed as $\Delta = \epsilon_{LUMO} - E_F$, where ϵ_{LUMO} and E_F are the LUMO of PVK pattern and Fermi level of Au, respectively. We estimated from the β values that the barrier height (Δ_1) of the 20-nm high structure is 60% that (Δ_2) of the 10-nm high structure ($\Delta_1/\Delta_2 = 2.3^{2/3}/4.9^{2/3} = 0.60$). The $\ln(I/V^2) \sim 1/V$ plot of the native PVK (see the inset of Figure 5d) does not obey the F−N law, probably because the F−N conduction mode is not activated in the 0−12 V voltage regime. Based on the HOMO−LUMO gap and $I-V$ characteristics, we suggest an F−N injection-limited mechanism for the electric conduction in the PVK patterns. The narrowing of HOMO−LUMO gap can lead to a reduction in energy barrier from Δ_0 of the native PVK to Δ of the PVK patterns (see the inset of Figure 5c). When the cross-linkage reaches a certain degree, Δ can be low enough to allow F−N electron injection. Higher PVK patterns correspond to a greater degree of cross-linkage and lower injection barrier and, therefore, facilitate a higher injection current. Similar F−N dominated carrier injection from metal to polymers has also been observed previously for other π-conjugated organic systems.[40−42]

In conclusion, we demonstrated the creation of polymeric PVK patterns with tunable electric functionality by AFM lithographically induced nanodischarge. The conductive structure formation is associated with the cross-linking of carbazole groups by bridge oxygen which significantly narrows the HOMO−LUMO gap of the patterned structures by forming extended conjugations. The larger conductivities measured for higher patterns originate from the reduced barrier height for F−N electron injection. By controlling the magnitude and duration of nanodischarge, both the morphology and conductivity of PVK patterns could be varied to meet different requirements. Our findings may open new routes to fabricating nanoscale heterogeneous structures with distinct chemical and physical characteristics from those of the matrix materials.

Acknowledgment. Mr. J. Subbiah and Mr. Y. W. Zhu are gratefully acknowledged for their help in the AFM experiments. This work is supported by NUS Nanoscience and Nanotechnology Initiative (NUSNNI), National University of Singapore.

Supporting Information Available: Experimental setup of large-scale discharge (S1), PES spectra of C 1s and N 1s core level emissions (S2), and DFT calculation results (S3). This material is available free of charge via the Internet at http://pubs.acs.org.

JA0577241

(34) Brédas, J. L.; Silbey, R.; Boudreaux, D. S.; Chance, R. R. *J. Am. Chem. Soc.* **1983**, *105*, 6555.
(35) Sze, S. M. *Physics of Semiconductor Devices*; Wiley: New York, 1981.
(36) Adamec, V.; Calderwood, J. H. *J. Phys. D: Appl. Phys.* **1975**, *8*, 551.
(37) Lenzlinger, M.; Snow, E. H. *J. Appl. Phys.* **1969**, *40*, 278.
(38) Okada, Y.; Iuchi, Y.; Kawabe, M.; Harris, J. S., Jr. *J. Appl. Phys.* **2005**, *88*, 1136.
(39) Zhang, Y.; Hu, Y.; Chen, J.; Zhou, Q.; Ma, D. *J. Phys. D: Appl. Phys.* **2005**, *36*, 2006.
(40) Tu, N. R.; Kao, K. C. *J. Appl. Phys.* **1999**, *85*, 7267.
(41) Kiy, M.; Biaggio, I.; Koehler, M.; Günter, P. *Appl. Phys. Lett.* **2002**, *80*, 4366.
(42) Parker, I. D. *J. Appl. Phys.* **1994**, *75*, 1656.